A Visible-Light-Enhanced Heterogeneous Photo Degradation of Tetracycline by a Nano-LaFeO$_3$ Catalyst with the Assistance of Persulfate

Liwei Hou [1,†], Yanan Wang [2,3,†], Fan Zhou [4], Shuangyue Liu [2], Lin Fu [2], Lei Wang [5,*], Changbo Zhang [2,*] and Weijie Xue [2,*]

1. College of Ocean Science and Engineering, Shanghai Maritime University, Shanghai 201306, China
2. Key Laboratory of Original Agro-Environmental Pollution Prevention and Control, Agro-Environmental Protection Institute, Ministry of Agriculture and Rural Affairs, Tianjin 300191, China
3. College of Resources and Environment, Northeast Agricultural University, Harbin 150030, China
4. College of Information Engineering, Shanghai Maritime University, Shanghai 201306, China
5. Key Laboratory of Environmental Biotechnology, Research Center for Eco-Environmental Sciences, Chinese Academy of Sciences, Beijing 100085, China
* Correspondence: leiwang@rcees.ac.cn (L.W.); zhangchangbo@caas.cn (C.Z.); tzfelicity@163.com (W.X.)
† These authors contributed equally to this work.

Abstract: Perovskites with nano-flexible texture structures and excellent catalytic properties have attracted considerable attention for persulfate activation in addressing the organic pollutants in water. In this study, highly crystalline nano-sized LaFeO$_3$ was synthesized by a non-aqueous benzyl alcohol (BA) route. Under optimal conditions, an 83.9% tetracycline (TC) degradation and 54.3% mineralization were achieved at 120 min by using a coupled persulfate/photocatalytic process. Especially compared to LaFeO$_3$-CA (synthesized by a citric acid complexation route), the pseudo-first-order reaction rate constant increased by 1.8 times. We attribute this good degradation performance to the highly specific surface area and small crystallite size of the obtained materials. In this study, we also investigated the effects of some key reaction parameters. Then, the catalyst stability and toxicity tests were also discussed. The surface sulfate radicals were identified as the major reactive species during the oxidation process. This study provided a new insight into nano-constructing a novel perovskite catalyst for the removal of tetracycline in water.

Keywords: nanoscaled LaFeO$_3$; visible light photocatalysis; tetracycline; acute toxicity

1. Introduction

Water contamination by pharmaceuticals has become an environmental issue of concern in recent decades. Most pharmaceuticals were directly excreted into domestic wastewater without effective treatment by conventional water treatment sites. Up until now, various kinds of drugs, such as antibiotics, hormones, and preservatives, have been identified within water environmental systems [1]. Because of their antibacterial natures, the antibiotic residues within contaminated waters cannot be effectively removed by traditional biological methods. The chemical a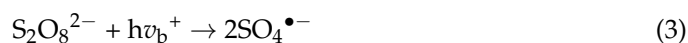dvanced oxidation processes (AOPs) for wastewater treatment appear then as reliable alternatives to biodegradation processes. AOPs involve the generation of hydroxyl radicals (•OH) [2–5]. In addition to hydroxyl-radicals-based reactions, some other AOPs, including peroxydisulfate-activated reactions, ultrasounds, UV-vis irradiation, and ozonation, have received great attention over the last decades [6–10]. In a "hybrid" AOP, consisting of visible light and the activation of peroxysulfate (PS), the sulfate radical was produced from the decomposition of persulfate ions (S$_2$O$_8^{2-}$) by using heat or even transition metal (Equations (1) and (2)) [7]:

$$S_2O_8^{2-} + heat \rightarrow 2SO_4^{•-} \tag{1}$$

$$S_2O_8{}^{2-} + Me^{n+} \rightarrow SO_4{}^{\bullet-} + SO_4{}^{2-} + Me^{(n+1)} \tag{2}$$
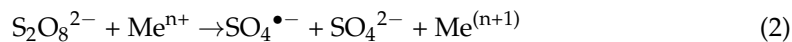
As shown in Equations (3)–(5), in sulfate-radicals-mediated photo-Fenton-like reactions, PS is an oxidant activated by the catalyst to produce reactive radicals ($SO_4{}^{\bullet-}$, $^{\bullet}OH$, and others), since it acts as an electron acceptor that can decrease the recombination between photogenerated electrons (e^-) and holes (h^+) [8]. Consequently, h^+ reacts with PS to generate $SO_4{}^{\bullet-}$ (Equation (3)). The formed e^- is able to decompose the PS to generate $SO_4{}^{\bullet-}$ (Equation (4)). In addition, the PS can be activated in the presence of visible light, generating $SO_4{}^{\bullet-}$ (Equation (5)). If a homogeneous ferrous catalyst is used, Fe^{2+} can be regenerated by the photogenerated e^-. However, the development of more efficient and stable photoactivation catalysts for sulfate-radical photo-Fenton processes is required.

$$S_2O_8{}^{2-} + hv_b{}^+ \rightarrow 2SO_4{}^{\bullet-} \tag{3}$$

$$S_2O_8{}^{2-} + e^- \rightarrow 2SO_4{}^{\bullet-} \tag{4}$$

$$S_2O_8{}^{2-} + hv \rightarrow 2SO_4{}^{\bullet-} \tag{5}$$

Perovskite-based oxides, of the general formula ABO_3, are important heterogeneous catalysts due to the low cost and flexibility of their composition, given their adjustable redox properties [11]. Therefore, they are especially studied within gas-phase catalytic depollution processes, including oxidation or reduction (CO, methane, VOCs, soot, and NO_x, etc.) [12–14]. Perovskites have been proposed as potential alternatives to the commercially used supported noble metals (mostly based on Pt, Pd formulations) [14]. Among the developed perovskites, iron-based compositions are found to present advantages for catalytic processes, due to their excellent high-temperature thermal and hydrothermal stability, redox activity, and the low cost of their constituting elements [15–18]. More interesting, in addition to their efficiency for gas-phase effluent treatments, perovskites can also serve as catalysts for wastewater treatment, due to the presence of transition metals with multiple valence states. It is reported, for example, that $BiFeO_3$-type perovskites (BFO) are active catalysts for oxidative acetylation [19], photocatalysis [20–26], hydrogen generation [27], and the catalytic activation of H_2O_2 [28]. $BiFeO_3/ZnFe_2O_4$ nanocomposites have also been employed as catalysts for the removal of azo dyes under visible light irradiation [28].

Owing to its stable crystal structure, excellent optical properties, and narrow bandgap (~2.1 eV), $LaFeO_3$ has been considered as a promising photoactive candidate. However, because $LaFeO_3$ is a p-type semiconductor, the rapid recombination of e^- and h^+ have been reported [29]. In addition, $LaFeO_3$ displays a low activity due to its high charge recombination rates. Therefore, introducing peroxides into the photocatalysis system may be an efficient strategy with the consideration of the capture effect of peroxides for photo-induced electrons on the conduction band of a photocatalyst. In this frame, it could be anticipated that the synergistic effects of the photocatalytic process and sulfate-radical-based performance could exhibit a higher degradation rate for organic pollutants than the Fenton process. As reported, peroxymonosulfate (PMS) was evidenced to be a good candidate for avoiding the recombination of e^- and h^+ and for improving the degradation efficiency of organic compounds [30–35]. Compared to H_2O_2, the longer O–O bond length and asymmetric structure of $HSO_5{}^-$ are supposed to guarantee the easier dissociation of PMS over organic compounds. However, some problems still remain, such as the limited catalytic activity of perovskite considering the low surface developed by the perovskites [11], the underutilization of PS [36], and the low stability of the catalyst with iron ions leaching occurring during the reaction [37].

From a fundamental point of view, textural properties, structural properties, and redox properties are interrelated parameters that have a significant effect on the catalytic performance of perovskites. However, using conventional methods for perovskite synthesis,

such as calcination milling [17] and even hydroxyacid complexation routes [38,39], lead to a large grain size (D), a low specific surface area (SSA), and a poor activity [24,25]. Indeed, when using a classical complexation approach [38,39], precursor complexation with hydroxyacid allows for the cations to be kept homogeneously dispersed in a hybrid matrix, ensuring crystallization at a lower temperature than that for solid–solid approach, i.e., 600–650 °C. Better catalytic performances are achieved in this last case due to improved textural properties, but an accessible surface area is not the only parameter affecting this catalysis, since the B-cation surface concentration, reducibility, and oxygen mobility of the catalysts are also considered to be key parameters [11,12,26]. Some improved synthetic approaches have then been proposed to obtain higher surface areas (30–100 m^2 g^{-1}) and smaller crystal sizes (<20 nm). Typical examples of these include the sol-gel-derived method [13], reactive grinding [40], nanocasting [41], and flame-spray pyrolysis [42], etc. Reactive grinding is an excellent example that allows for the production of high-surface-area materials (reported to reach 100 m^2 g^{-1} [43]), but its popularization is restricted due to the requirement of special equipment, and this approach is better adapted to large-scale synthesis than laboratory-scale synthesis [44,45]. However, it is still a real challenge to directly synthesize size-limited and pure nanocrystalline perovskites with particular porosities. A benzyl alcohol (BA) route was proposed as a valuable approach for oxide and mixed oxide nanoparticle preparations. This route not only offers an excellent control over the particle size, shape, crystallinity, order, purity, and assembly behavior, but also avoids the use of any additional surfactants or templates [46–49]. The BA route is defined as a non-aqueous synthesis, since during the different competitive reactions, no water is added, which affords a better control over the crystal assembly.

In this work, nano-$LaFeO_3$ was prepared by a citric acid complexation route and benzyl alcohol route. Using an adapted synthesis procedure [49], the benzyl-alcohol-derived material presented quasi-spherical nanosized particles with a much higher specific surface area, as well as a lower crystal size domain size. The reaction parameters for the sulfate-radical–photo-Fenton tetracycline degradation process were optimized (operating pH, oxidant concentration, and catalyst loading) with this catalyst. The catalyst stability was also evaluated upon the reaction cycling, which was followed by metal ion leaching.

2. Materials and Methods

2.1. Materials and Methods

The synthesis was performed by a benzyl alcohol route.

The sample $LaFeO_{3\_}BA$: $La(NO_3)_3 \cdot 6H_2O$ (2 mmol) was dissolved in anhydrous benzyl alcohol (26.7 mL) at room temperature. After that, iron (III) acetylacetonate (2 mmol) was added dropwise into the benzyl alcohol (40 mL) at room temperature. The reaction mixture was thereafter stirred for 30 min and transferred into a Teflon-lined autoclave. The autoclave was heated to 200 °C for 24 h. The resulting brown suspension was recovered by centrifugation (4 cycles, with washing with ethanol between each cycle). The centrifugation was performed at 8000 rpm for 10 min. The washed material was dried at 80 °C for 12 h, and the dry solid was calcined at 500 °C for 6 h. The prepared sample was labeled as the BA sample.

The synthesis was then performed by a citric acid complexation route.

The sample $LaFeO_{3\_}CA$: aqueous solutions of lanthanum(III) nitrate hexahydrate (20 mM) ($LaNO_3 \cdot 6H_2O \geq 99.0$ %, Sigma-Aldrich, Houston, USA) and iron(III) nitrate hexahydrate (20 m mol L^{-1}) (97.7%, Alfa Aesar, Shanghai, China) were prepared with distilled water. Thereafter, an aqueous solution of citric acid (98 %, Prolabo, Paris, France), with a molar equivalence to La + Fe (40 mmol L^{-1}), was added dropwise to the precursor solution under gentle stirring at 80 °C. Ageing was performed until a gel was obtained. The gel was thereafter dried in an oven at 110 °C for 12 h. Subsequently, the obtained foam solid was crushed and calcined at 500 °C for 6 h. The sample was labeled as the CA sample.

2.2. Experimental

The reaction configuration: the experiment was carried out in a photo-reactor consisting of visible LED lamps, as shown in Figure 1. The LED lamp emitted white light at a wavelength of 455 nm and further broadband stokes-shifts were emitted at roughly 500–600 nm.
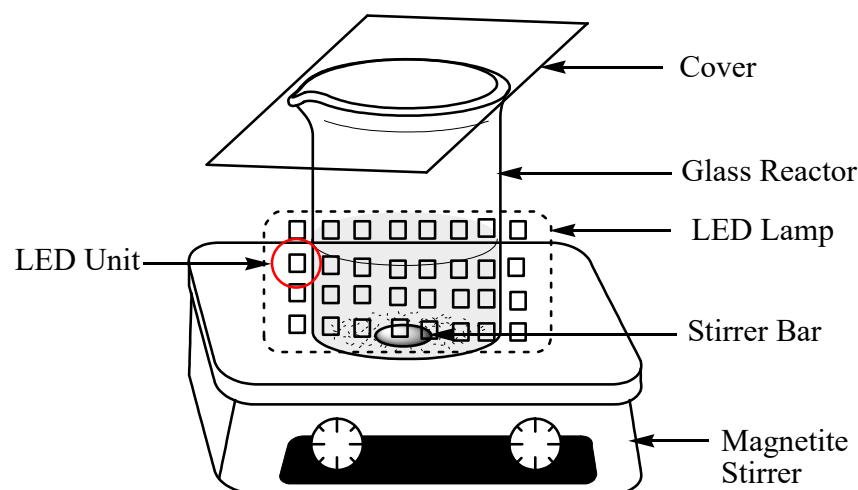

Figure 1. Scheme of the experimental reaction configuration with a LED strip as light source.

For the activity measurement, a solution of tetracycline (TC, purity, and source) was prepared with deionized water (in the two hours preceding the reaction). The initial concentration (C_0) was fixed at 100 mg L^{-1} and the C_0 exact value was verified by an HPLC analysis. Then, a selected weight of the $LaFeO_3$ was added into 200 mL of the TC solution, with constant stirring that was maintained using a mechanical stirrer (RW 20, IKA, Staufen, Germany) for 15 min, in order to achieve adsorption–desorption equilibrium on the solid catalyst surface. At this time, the $[TC]_0$ value—the concentration of the TC after the adsorption process—was obtained. Then, a persulfate (PS) solution, prepared by the dissolution of 1 mol L^{-1} (purity and source) in water to obtain a PS concentration of 50 mmol L^{-1}, was added to start the reaction. All the experiments were conducted at ambient temperature (22 ± 2 °C). The reaction solution was sampled (1 mL) over fixed intervals and mixed with 1 mL of methanol (0.1 mol L^{-1}) for at least 15 min to terminate the reaction. Then, the reaction solution was filtered through a 0.22 μm membrane (Millipore Co., Molsheim, France) and mixed with the same volume of methanol to quench the reaction. The TC conversion (X_{TC}) and the total organic carbon (TOC) abatement (X_{TOC}) were calculated by Equations (6) and (7), respectively.

$$X_{TC} = \frac{C_0 - C}{C_0} \times 100\% \tag{6}$$

$$X_{TOC} = \frac{TOC_0 - TOC}{TOC_0} \times 100\% \tag{7}$$

where C is the TC concentration at time t (min), TOC is the total organic carbon time t (min), and TOC_0 is the initial total organic carbon after stabilization due to the adsorption on the catalyst surface.

2.3. Characterization and Analysis

X-ray diffraction (XRD) was performed. The X-ray diffraction patterns were obtained on a D5005 diffractometer (Bruker, Karlsruhe, Germany) equipped with Cu Kα radiation (λ = 1.5406 Å). The signal was recorded for 2θ between 20° and 80°, with a recording step of 0.05° (3 s per step). A phase identification was performed by a comparison with the JCPDS

database. The crystal size was determined using the Scherrer equation after applying Warren's correction for the instrumental broadening.

For the N_2-physisorption, N_2 adsorption measurements were performed on a Micromeritics TRISTAR 3000 instrument. A desorption isotherm was used to determine the pore size distribution using the Barret Joyner Halenda (BJH) method. The specific surface areas (SSA) of the catalysts were obtained by applying the Brunauer–Emmett–Teller (BET) equation ($0.10 < P/P_0 < 0.35$). Prior to the analysis, the samples (0.5 g) were heated at 250 °C under a vacuum for 6 h.

The specific surface area (ssa) can then be derived:

$$ssa = \frac{V_m N_A a_m}{v_m m_s} \tag{8}$$

where N_A is the Avogadro's number (6.022×10^{23} mol^{-1}), a_m is the effective cross-section area of one adsorbed molecule, v_m is the molar volume of one adsorbed molecule (22,400 mL of the volume occupied by 1 mol of the adsorbate gas under standard conditions), and m_s is the mass of the substrate/adsorbent.

Then, transmission electron microscopy (TEM) was used. The catalyst morphology was determined by a TEM analysis coupled with energy-dispersive X-ray spectroscopy (EDXS). The micrographs were collected on a JEM 2100 instrument (JEOL, Tokyo, Japan), operated at 200 kV with a LaB6 source and equipped with a Gatan Ultra scan camera. The EDX spectroscopy was carried out with a Hypernine (Premium, JEOL, Japan) detector (active area: 30 mm^2), using the SM-JED 2300T software for the data acquisition and treatment.

All the catalysts were systematically characterized using X-ray diffraction (XRD), X-ray photoelectron spectroscopy (XPS), N_2-physisorption, and ICP-OES (see the Supplementary Data for details).

The tetracycline concentration was determined by using a high-performance liquid chromatography (HPLC) instrument that was equipped with an Aminex HPX-87 (BioRad, Hercules, CA, USA) column. The TOC content was determined using a TOC meter. The concentration of the PS was analyzed with an iodometric titration method, according to the procedure described in ref [6]. The amount of leached iron was determined by an analysis of the Fe ion concentration in the aqueous phase. Spectrophotometry at λ = 510 nm, after adding 1,10-phenanthroline to form an iron–phenanthroline complex, was used. Finally, the stability and reusability of the catalyst were evaluated.

3. Results and Discussion

3.1. Physicochemical and Structure Properties

The samples that were prepared by non-aqueous benzyl alcohol routes (BA) and citrate complexation routes (CA) showed reflections that were characteristic of the perovskite phase (Figure 2), being in perfect agreement with the orthorhombic structure of $LaFeO_3$ (JCPDS card 74-2203). A small, broad, and poorly defined reflection of 28.220° (101) was visible on the baseline of the BA sample pattern. This reflection was identified in the $La(OH)_3$ external phase, according to the JCPDS reference JCPDS No. 36-1481. The larger FWHM of the XRD peaks observed for the BA sample show that this material presented a lower crystal size than the CA sample at the iso-crystallization temperature (18.4 nm for BA vs. 22.3 nm for CA): an 18% lower crystal size was measured for the BA. These results confirm that the BA route was adapted for the production of crystalline-mixed oxide nanoparticles, starting from an organic–inorganic hybrid precursor [50]. A larger specific surface area (32.5 m^2 g^{-1}) was also obtained for the BA sample, which was much higher than the value for the $LaFeO_3$ sample that was obtained by the CA route (15.3 m^2 g^{-1}), with a 112% higher SSA.
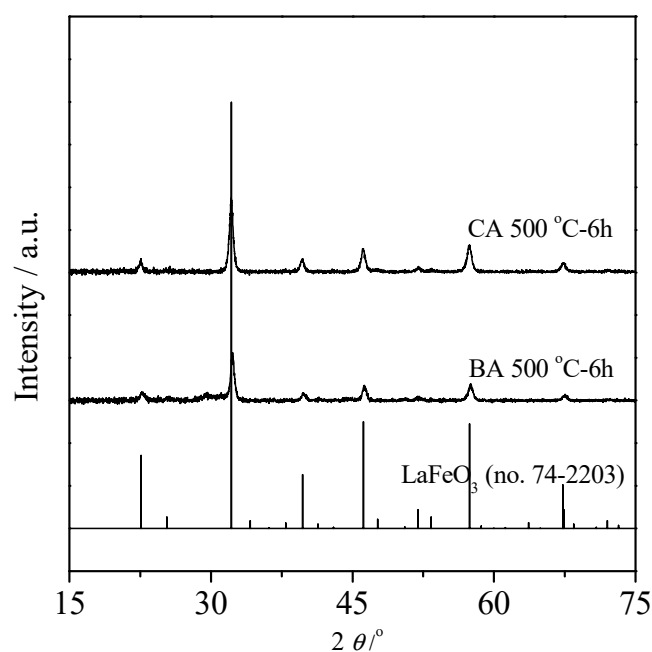
Figure 2. XRD results for LaFeO$_3$ samples prepared by the BA and CA routes. Bottom of the figure: vertical lines for reference LaFeO$_3$ (JCPDS card 74-2203).

Starting from the value of the average crystal domain size obtained from the XRD, it is possible to calculate a theoretical surface area, assuming a cubic-shaped crystal and no contact between the adjacent elementary particles. Then, a ratio R between the experimental specific surface area and the theoretical surface area ($R = S_{BET}/S_{th}$, Table 1) gives an indication of the agglomeration degree of the elementary crystals in the different materials.

Table 1. Selected physico-chemical characteristics obtained for BA and CA catalysts.

Samples	BA Sample	CA Sample
Chemical composition	La$_x$Fe$_y$O$_{3\pm\delta}$	La$_x$Fe$_y$O$_{3\pm\delta}$
D_{XRD}/[a] nm	18.4	22.3
S_{th}/[b] m^2 g^{-1}	49.2	36.9
S_{BET}/[c] m^2 g^{-1}	32.5	15.3
R/[d] -	0.66	0.41

[a], D_{XRD} is the crystal domain size determined using the Scherrer equation after correction of the FWHM for instrumental broadening; [b], S_{th} is the theoretical surface area calculated from the surface area developed by a cubic particle volume of separated single crystal grains of D_{XRD} size, assuming no contact between adjacent particles (no agglomeration); [c], S_{BET} is the surface area determined using the B.E.T. equation; and [d], $R = S_{BET}/S_{th}$, characterize the degree of agglomeration in the material ($R = 1$, no agglomeration).

Then, when $R = 1$, the developed surface area is equal to the theoretical surface area, which characterizes a poorly agglomerated material. When R approaches 0, meaning that the theoretical surface area is larger than the experimental specific surface area, dense and poorly porous agglomerates are occured in the material [51,52]. A comparison between the R ratios obtained for the two samples showed that the BA sample presented a significantly higher ratio compared to that of the CA sample. This result indicates that the BA route prevented the potential agglomeration of the perovskite, leading to a greater accessible surface area.

The morphologies of the BA and CA LaFeO$_3$ samples were investigated by TEM (Figure 3).
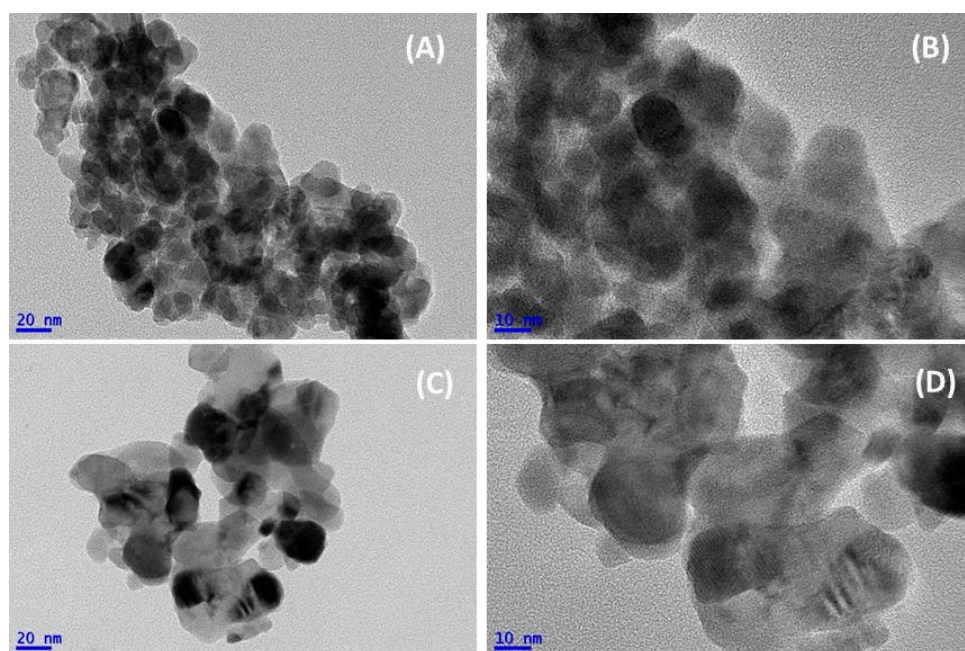
Figure 3. TEM images of BA catalyst (**A**,**B**), and CA catalyst (**C**,**D**) samples, after thermal stabilization at 500 °C.

Based on the images in Figure 3A,B, the LaFeO$_3$ sample that was synthesized via the BA route was composed of almost spherical LaFeO$_3$ nanoparticles, with diameters ranging from 10 to 30 nm. These observed sizes were consistent with the average crystal domain sizes determined by the XRD (18.4 nm). The elementary particles formed small agglomerates, in which the presence of contrasted zones evidenced the formation of internal porosity. Slight differences were observed for the CA sample. While the low-magnification images evidenced the formation of agglomerates of more comparable sizes than those for the BA sample (Figure 3C), the high-magnification observation evidenced the agglomeration of elementary particles of sizes between 10 and 80 nm (Figure 3D). The particles showed inhomogeneity in their sizes and shapes. This morphology, mostly that of the larger average particle size, was at the origin of the lowest SSA (15.3 m^2 g^{-1}).

3.2. Process Configuration Effect on the Degradation of the TC Degradation

Different configurations of the process were tested to evaluate their respective efficiencies in the TC degradation reaction (Figure 4):

- The PS alone (single process);
- The catalyst alone (single process);
- A combination of visible light/PS (dual process);
- A combination of PS/BA (dual process);
- A combination of visible light/BA (dual process);

For the combination of visible light/PS/BA (ternary process), the quantum yield was estimated to examine the photodegradation efficiency [53], which was found to be 2.3×10^{-2}.

The photo stability of the tetracycline was also assessed. In order to explore the individual contribution of the photo-catalysis to the removal of the TC, the TC solution was irradiated by visible light alone until the equilibrium concentration of the TC, [TC]$_0$, was obtained. A 15.5% decrease in the TC concentration was obtained by photolysis, given a [TC]$_0$ value of 98.9 mg L^{-1} (corrected concentration). The retaining of more than 80% of the initial concentration evidenced the resistance of the TC toward to photo-catalytic degradation under visible irradiation alone.
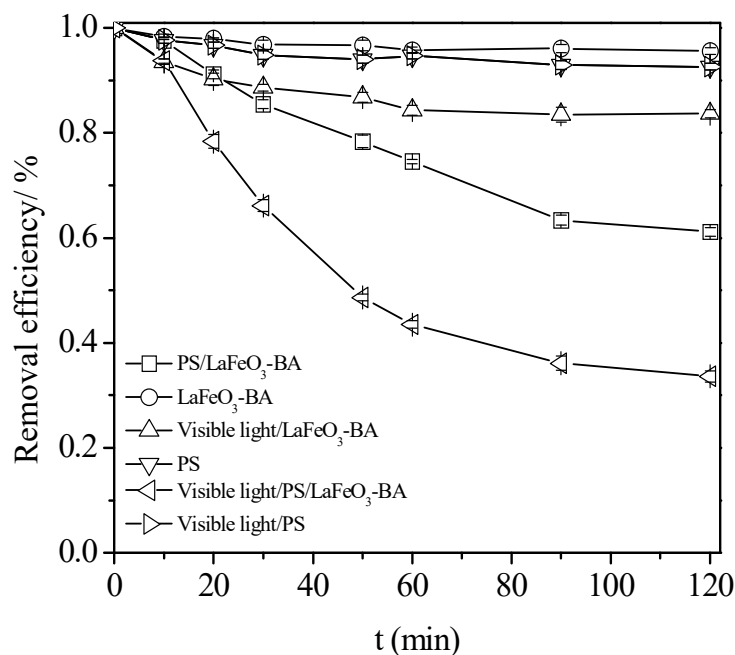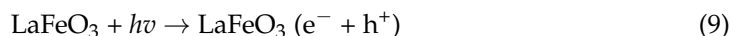
Figure 4. Process combination effect on the tetracycline degradation. Conditions: C_0 = 100 mg L^{-1}, [BA] = 0.5 g L^{-1}, [PS] = 50 mM, and pH$_0$ = 3.7.

In the single processes (PS or catalyst alone), the TC chemical degradation rate remained very slow under the selected operating conditions (22 °C, pH = 3.7). At the end of the reaction time, i.e., t = 120 min, the remaining concentration of the TC stayed above 92% of the [TC]$_0$ value (Figure 4). The experiments realized with only the BA catalyst added to the solution also demonstrated a very limited efficiency, with the value of the TC concentration's decrease remaining below 20%. Such an abatement (<10%) then demonstrates the limited ability of the catalyst surface for the simple adsorption of the organic pollutant.

Among the three configurations of the dual processes, the least efficient was the visible light/BA configuration, with an abatement that was limited to 14%, which is not surprising considering that, in this configuration, no efficient oxidant was added. Then, a slightly better efficiency was reached with the dual visible light/PS configuration, with a TC concentration abatement of 30% that was obtained after 120 min. However, this result shows that the process was poorly efficient when considering the stoichiometry of the reaction, being in excess of the PS (molar ratio PS/TC = 208.3) to afford the complete degradation of the pollutant. The best results were obtained during the last dual process, the coupling of PS and BA without light irradiation: a TC concentration abatement of 39% was obtained after 120 min. These results clearly indicate that the PS could be activated by the LaFeO$_3$ to generate active radical oxidants.

When perovskites are irradiated with visible light energy that is equivalent to their band gap energy, the generation of photo-generated electrons and holes takes place. These photo-generated electrons and holes then participate in series of reactions and lead to the generation of active radical species (•OH), as shown below in Equations (9)–(13).

$$LaFeO_3 + h\nu \rightarrow LaFeO_3\ (e^- + h^+) \tag{9}$$

$$e^- + O_2 \rightarrow O_2^{\bullet-} \tag{10}$$

$$O_2^{\bullet-} + H^+ \rightarrow HO_2^{\bullet} \tag{11}$$

$$2e^- + HO_2^{\bullet} + H^+ \rightarrow {}^{\bullet}OH + OH^- \tag{12}$$

$$h^+ + OH^- \rightarrow {}^\bullet OH \tag{13}$$

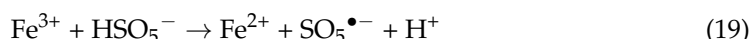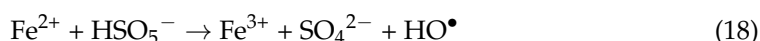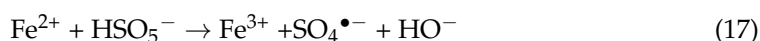$$h^+ + H_2O \rightarrow H^+ + {}^\bullet OH \tag{14}$$

Additionally, these photo-generated electrons and holes (h^+) can undergo reactions with PS to enhance the production of $SO_4{}^{\bullet-}$, as shown below in Equations (14) and (15):

$$e^- + S_2O_8{}^{2-} \rightarrow SO_4{}^{\bullet-} + HO^- \tag{15}$$

$$h^+ + HO^- \rightarrow {}^\bullet OH \tag{16}$$

Besides the role of photocatalysis, the activation of PS on the iron oxide surface induces the formation of radicals, including $SO_4{}^{\bullet-}$ (Equations (17)–(19)) via a reaction on the catalyst surface [34], which will thereafter react with the TC. From a mechanistic point of view, ref. [35] demonstrated that the formation of these radicals involves an Fe^{3+}/Fe^{2+} redox cycle, according to the following equations:

$$Fe^{2+} + HSO_5{}^- \rightarrow Fe^{3+} + SO_4{}^{\bullet-} + HO^- \tag{17}$$

$$Fe^{2+} + HSO_5{}^- \rightarrow Fe^{3+} + SO_4{}^{2-} + HO^\bullet \tag{18}$$

$$Fe^{3+} + HSO_5{}^- \rightarrow Fe^{2+} + SO_5{}^{\bullet-} + H^+ \tag{19}$$

Thereafter, the formed radicals (sulfate and/or hydroxyl) can attack the TC molecules and the TC molecules can be directly oxidized by the ${}^\bullet OH$ and $SO_4{}^{\bullet-}$, thus generating by-products. These detected intermediates are then, to some extent, further mineralized to CO_2 (Equation (20)).

$${}^\bullet OH/SO_4{}^{\bullet-} + TC \leftrightarrow \text{intermediates} \leftrightarrow CO_2 + H_2O + SO_4{}^{2-} \tag{20}$$
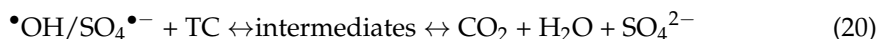
For the ternary process, when compared to the dual conditions, the degradation efficiency largely increased upon the visible irradiation being added to the coupled PS/BA. Indeed, the apparent constant rate value, k_{app} (calculated assuming a pseudo-first-order reaction, list the different hypotheses), that was measured for the visible light/PS/BA was 0.0218 min^{-1}, which was more than 6.8 times than the sum of the k_{app} obtained for the visible light/PS (0.0032 min^{-1}) and PS/LaFeO$_3$ (0.0050 min^{-1}). Especially compared to LaFeO$_3$-CA (LaFeO$_3$ syntheses by a citric acid complexation route), the pseudo-first-order reaction rate constant increased by 1.8 times. This indicated the synergistic effect of coupling the three conditions on the TC degradation rate. Furthermore, we evaluated the decomposition of the added PS that took place during the reaction. The utilization degree of the PS was 63% in the ternary visible light/PS/BA process, while it was only 21% for the dark dual PS/BA process. TC can absorb visible light energy into the excited state, facilitating an electron transfer to the Fe^{3+} surface site and resulting in PS decomposition into $SO_4{}^{\bullet-}$ radicals, with an associated reduction in the iron surface site that is available on the catalyst surface, as proposed the above in Equations (16)–(18).

In order to confirm this mechanism (surface activated/dependent or not), the CA and BA catalysts were tested under comparable conditions (Figure 5). While a k_{app} of 0.0218 min^{-1} was obtained with the BA catalyst, a value of 0.0122 min^{-1} was obtained with the CA catalyst.
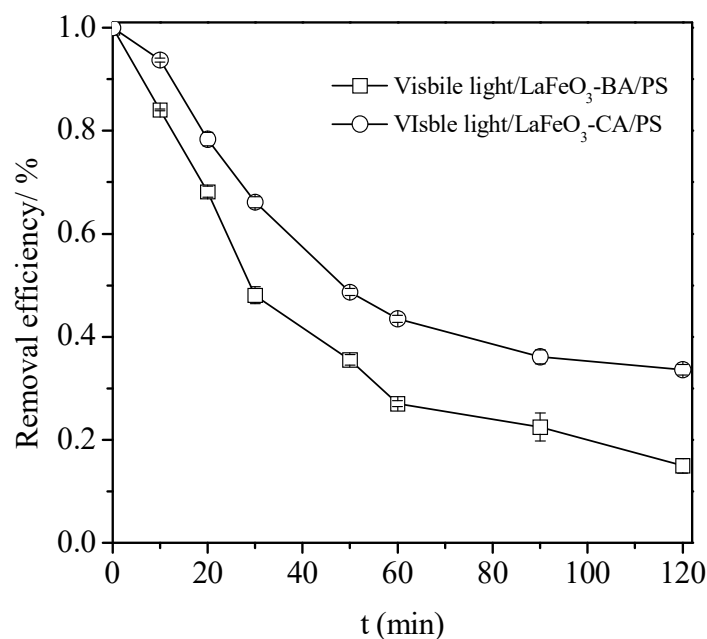
Figure 5. Impact of the preparation method on the catalyst efficiency in the visible light/PS/catalyst process for the tetracycline degradation. Conditions: C_0 = 100 mg L^{-1}, catalyst (BA or CA) = 0.5 g L^{-1}, [PS] = 50 mmol L^{-1}, and pH_0 = 3.7.

This result demonstrated the beneficial effect of using a BA catalyst instead of a CA catalyst. Considering the surface-activated mechanism for oxidant radical formation, both the surface area (being higher for the BA, Table 1) and the Fe^{3+} surface site's reducibility (also being higher for the BA) were expected to be at the origin of the highest performances obtained with the BA catalyst. TPR experiments indeed demonstrated an activation of the Fe^{3+} surface site with the BA at a temperature of approx. 400 °C below the temperature that was obtained for the CA, which was already obtained by our previous results on the oxygen mobility/reducibility of iron-based perovskites produced by a benzyl alcohol route [44].

3.3. Operating Parameter Impact on the Process Global Efficiency

3.3.1. Catalyst Dosage and Oxidant Concentration Effect

The effect of the concentration of the BA on the TC degradation efficiency was also investigated (Figure 6). It was found that the TC removal efficiency and k_{app} increased with an increase in the catalyst loading when it increased from 0.1 g L^{-1} to 0.5 g L^{-1}. At a BA loading of 0.5 g L^{-1}, an 83.9% abatement of the $[TC]_0$ was obtained after 120 min, corresponding to a k_{app} of 0.0218 min^{-1}. A further increase of catalysts loading (BA) did not improve the TC abatement (84%) after 120 min.

The effects of the oxidants and PS concentrations on the degradation of the TC are presented in Figure 7 and also show that an increase in the oxidant concentration is beneficial to the TC abatement.

In this last case, the k_{app} value was linearly dependent on the PS concentration. Then, in the interval of the optimization selected, the catalyst loading and initial PS concentration values that led to the highest TC abatement, at a pH of 3.7, were 0.5 g L^{-1} and 50 mmol L^{-1}, respectively.
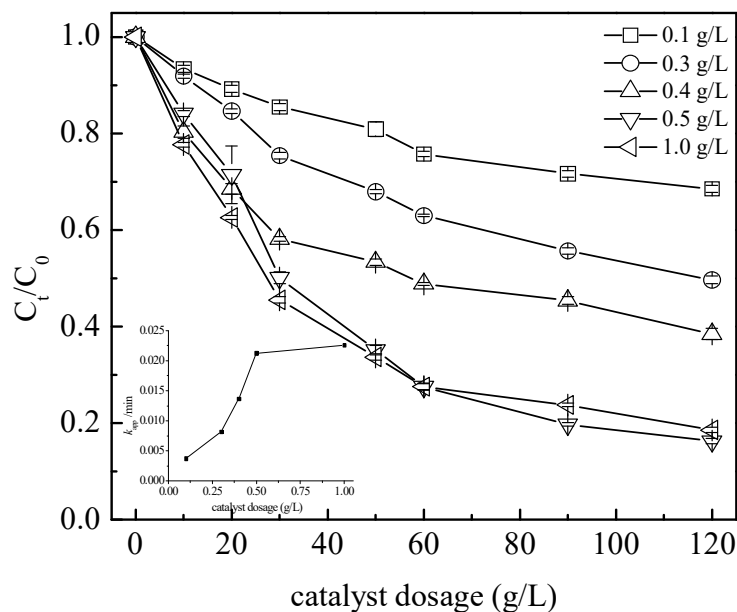
Figure 6. Effect of the BA catalyst dosage on the TC degradation. Conditions: $C_0 = 100$ mg L^{-1}, [PS] = 50 mM, and pH$_0$ = 3.7.

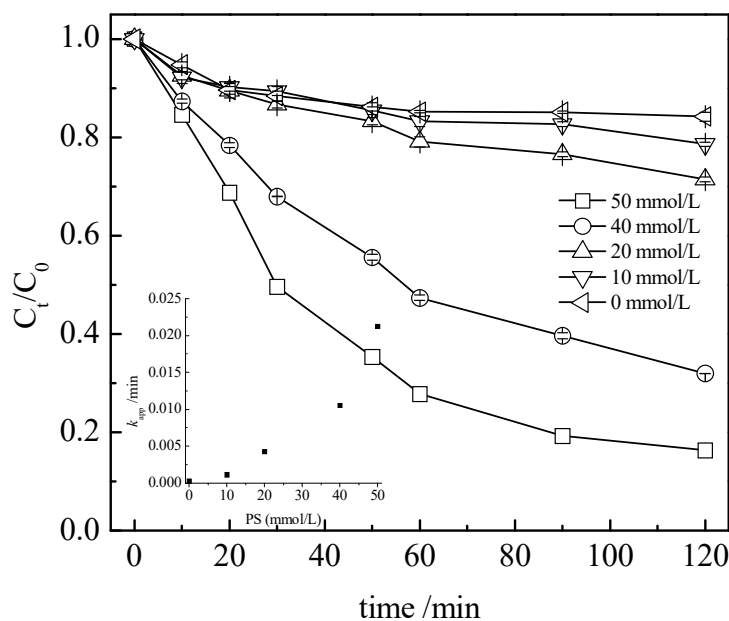**Figure 7.** Effect of the sodium persulfate concentration on the tetracycline degradation. Conditions: $C_0 = 100$ mg L^{-1}, [BA] = 0.5 g L^{-1}, and pH$_0$ = 3.7.

3.3.2. pH Value Effect

To investigate the pH effect on the degradation of the tetracycline, three different values of the initial pH (3.7, 7.0, and 9.0) were tested under acidic, neutral, and basic conditions. The results presented in Figure 8 show that the calculated TC removal efficiency and k_{app}, assuming a first-order reaction rate, decreased accordingly with an increase in the pH value.
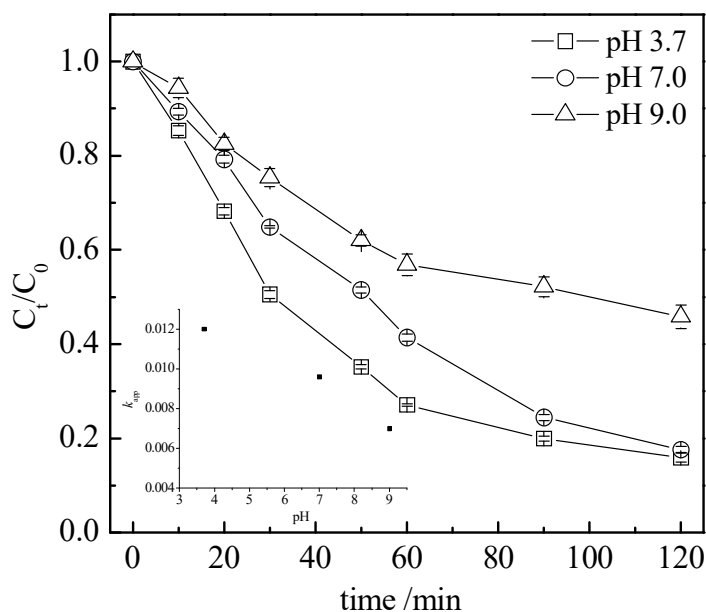
Figure 8. Effect of reaction medium initial pH on the tetracycline degradation. Conditions: $C_0 = 100$ mg L^{-1}, [BA] = 0.5 g L^{-1}, and [PS] = 50 mmol L^{-1}.

When compared to the value obtained at pH = 3.5 (k_{app} = 0.012 min^{-1}), the value of the k_{app} decreased by 20% at pH = 7.0 to 0.0096 min^{-1}. While the k_{app} decreased significantly, the final TC abatement value was 82.3% after 120 min, which was very close to the value obtained at pH = 3.5, i.e., 83.9%. From a mechanism point of view, carboxyl acids (such as acetic acid) are produced during the reaction. Therefore, when the TC is degraded, the production of acidic intermediates induces a pH value decrease in the reaction medium when the reaction is performed without a buffer solution (such as in our case). This explains why, with a reaction starting at pH = 3.7, a final pH value of 2.6 was obtained after 120 min of the reaction. In the case of an initial pH of 7.0, the final value obtained was 2.7. Then, starting from 3.7 or 7.0, the final pH values of the reaction were comparable, explaining why comparable TC abatements were obtained in the two cases. The lowest value of the k_{app}, 0.0073 min^{-1}, was obtained when the initial pH value was increased to 9.0 and the TC abatement reached only 53%, a value far below the 82.3–83.9% obtained at the pHs of 3.7 and 7.0. In the case of an initial pH of 9.0, the pH value obtained at the end of the reaction was 4.2. These results demonstrate that the reaction was far more efficient in acidic conditions. However, the choice to perform the reaction without any buffer (such as NaHCO$_3$/KHSO$_4$ or Na$_2$HPO$_4$/KH$_2$PO$_4$) originated from the fact that buffer ions may act as scavengers of radicals such as SO$_4$$^{\bullet -}$, as demonstrated in Equations (21) and (22) [44]:

$$SO_4^{\bullet -} + HCO_{3-} \rightarrow SO_4^{2-} + HCO_3 \tag{21}$$

$$HCO_3 + H^+ \leftrightharpoons CO_3^{2-} \tag{22}$$

3.4. Catalyst Stability Test

The BA catalyst stability was investigated by the means of recycling experiments: the BA catalyst was repeatedly used in five successive batch experiments, as shown in Figure 9. After each run, the BA catalyst in the reaction solution was centrifuged, recovered, and dried at 100 °C for 12 h. The dried powder was directly used for the next reaction cycle, applying exactly similar conditions to those for the first run.
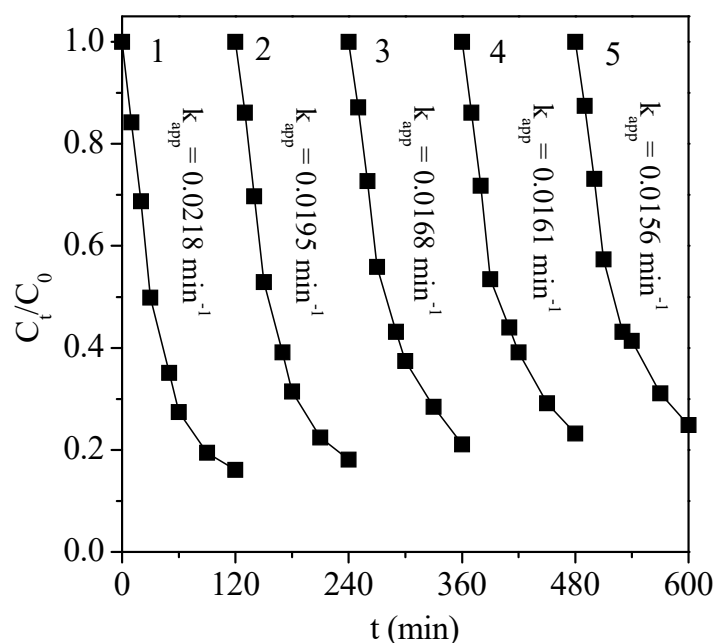
Figure 9. Evolution of the BA catalyst activity with the reaction cycles of TC degradation under visible light/PS/catalyst coupled process. Conditions: $C_0 = 100$ mg L^{-1}, [PS] = 50 mmol L^{-1}, [BA] = 0.5 g L^{-1}, and pH$_0$ = 3.7.

As can be observed in Figure 9, the BA was capable of being reutilized for at least five cycles, and the reused catalyst retained an acceptable catalytic activity. After the third cycle, the total removal efficiency of the TC was 83.9% at the first cycle. At the fifth cycle, the TC abatement always reached 79.3%. At this fifth cycle, the TC removal efficiency and the leached iron concentration were also evaluated. In addition, we also tested the TOC value. The result found that the TOC removal efficiency was 54.3%, which was an excellent level of mineralization considering the difficulty of degrading TC molecules. Furthermore, the leaching of Fe and La from LaFeO$_3$ was also evaluated, quantifying the dissolved Fe and La in the reaction medium by ICP-OES: [La] = 0.03 mg L^{-1} and [Fe] = 0.02 mg L^{-1}. This corresponded to a very limited leaching of the elements from the catalyst, in accordance with the maintenance of an excellent abatement during the five successive cycles at pH 3.7. To validate the heterogeneous character of the reaction, the reaction was performed with iron and lanthanum, which were added by the dissolution of nitrate precursors at the same concentrations as those obtained in the final reaction medium. A TC abatement of 3.81% was obtained after 120 min, which can be considered negligible in comparison to the 83.9% obtained in the presence of the catalyst. Then, this result confirmed the absence of a contribution of the dissolved species (either Fe or La) to the efficiency measured. It also allowed for the conclusion of a heterogeneous, mediated reaction, in which the nano-LaFeO$_3$ behaved as an efficient and stable system when coupled with persulfate and visible irradiation.

3.5. Toxicity Evolution

Even though 83.9% of the TC was converted in the visible light/LaFeO$_3$-BA/PS process after 120 min, the TOC conversion of the TC was only 54.3%. In this case, the variation in the acute toxicity was evaluated by a 48 h immobilization assay with *D. magna*. A 60% mortality rate of the *D. magna* was reached with a raw TC solution. After a 120 min reaction in the visible light/LaFeO$_3$-BA/PS system, the toxicity reached a maximum value and 100% of the *D. magna* was immobilized, indicating that the formation of primary degradation by-products had a considerably higher toxicity than the TC. When the reaction time was extended to 240 min, the inhabitation percentage decayed, i.e., the mortality

rate was only 45%. Therefore, prolonging the reaction time to reduce its acute toxicity is necessary for the TC treatment.

4. Conclusions

Tetracycline in an aqueous solution was efficiently degraded by a visible light/heterogeneous $LaFeO_3$/persulfate process. The use of nano-$LaFeO_3$ perovskite and visible LED lamps provided sensible advantages, including: (i) a low cost for the heterogeneous catalyst, (ii) convenient operation conditions (ambient temperature and no pressure), and (iii) a low power consumption (LED lamps irradiation). The properties of the nano-$LaFeO_3$, especially its surface area, impact the efficiency of the global process. The other parameters influencing the final tetracycline degradation degree are: the catalyst loading, the persulfate loading, and the reaction medium pH. Satisfying the stability of the catalyst is obtained upon the reaction cycling, with a very limited leaching of the La and Fe. Nano-$LaFeO_3$ can be considered to be an efficient heterogeneous catalyst, allowing for the use of persulfate as an oxidant to replace the more classically used H_2O_2, in view of the pollutant degradation in water.

Author Contributions: Writing—original draft preparation, conceptualization, methodology, L.H. and Y.W.; software, F.Z.; validation, S.L. and L.F.; formal analysis, L.W. and W.X.; project administration, funding acquisition, L.W. and C.Z. All authors have read and agreed to the published version of the manuscript.

Data Availability Statement: Not applicable.

Conflicts of Interest: The inefficient Fe(III)/Fe(II) cycle and high persulfate dosage severely restricted the practical application prospects of the persulfate activation. The development of a novel heterogeneous catalyst with a high surface area, high Fe(III)/Fe(II) cycle, and in situ persulfate generation is of significance in the wastewater advance oxidation process. In this study, we designed and fabricated a nano-sized $LeFeO_3$ as an efficient persulfate activator. Tetracycline in an aqueous solution was efficiently degraded by a visible light/heterogeneous $LaFeO_3$/persulfate process. The low power consumption (LED lamps irradiation) is adaptable for industry utilization. The surface oxygen vacancies of $LaFeO_3$ as photo-generated electron transfer mediators enhance the redox cycle efficiency of Fe(II)/Fe(III). The interfacial reaction mechanism experiment indicates that the surface sulfate radicals groups participate in the persulfate activation as the main active sites. We believe this study provides a facile route for efficient persulfate activation and strengthens the inconvenient role of in situ persulfate generation on pollutants degradation.

References

1. Ogunlaja, A.; Ogunlaja, O.O.; Olukannia, O.D.; Taylor, G.O.; Olorunnisola, C.G.; Dougnon, V.T.; Mousse, W.; Fatta-Kassinos, D.; Msagati TA, M.; Unuabonah, E.I. Antibiotic resistomes and their chemical residues in aquatic environments in Africa. *Environ. Pollut.* **2022**, *312*, 119783. [CrossRef]
2. Do, S.H.; Jo, J.H.; Jo, Y.H.; Lee, H.K.; Kong, S.H. Application of a peroxymonosulfate Cobalt (PMS/Co(II)) system to treat diesel-contaminated soil. *Chemosphere* **2009**, *77*, 1127–1131. [CrossRef] [PubMed]
3. Rastogi, A.; Al-Abed, S.R.; Dionysiou, D.D. Sulfate radical-based ferrous–peroxymonosulfate oxidative system for PCBs degradation in aqueous and sediment systems. *Appl. Catal. B Enivron.* **2009**, *85*, 171–175. [CrossRef]
4. Kolthoff, I.M.; Miller, I.K. The chemistry of persulfate. I. The kinetics and mechanism of the decomposition of the persulfate ion in aqueous medium. *J. Phys. Chem. B* **1951**, *73*, 3055–3059.
5. Anipsitakis, P.G.; Stathatos, E.; Dionysiou, D.D. Heterogeneous Activation of Oxone Using Co_3O_4. *J. Phys. Chem. B* **2005**, *109*, 13052–13055. [CrossRef]
6. Cai, C.; Zhang, H.; Zhong, X.; Hou, L. Ultrasound enhanced heterogeneous activation of peroxymonosulfate by a bimetallic Fe–Co/SBA-15 catalyst for the degradation of Orange II in water. *J. Hazard. Mater.* **2015**, *283*, 70–79. [CrossRef]
7. House, D.A.; House, D.A. Kinetics and mechanism of oxidations by peroxydisulfate. *Chem. Rev.* **1962**, *62*, 185–203. [CrossRef]
8. Wang, Y.; Liu, C.; Zhang, Y.; Meng, W.; Yu, B.; Pu, S.; Yuan, D.; Qi, F.; Xu, B.; Chu, W. Sulfate radical-based photo-Fenton reaction derived by $CuBi_2O_4$ and its composites with α-Bi_2O_3 under visible light irradiation: Catalyst fabrication, performance and reaction mechanism. *Appl. Catal. B Enivron.* **2018**, *235*, 264–273. [CrossRef]

9. Chudzińska, J.; Woźniak, B.; Sprynskyy, M.; Nowak, I.; Feliczak-Guzik, A. Photoremoval of bisphenol A using hierarchical zeolites and diatom biosilica. *Int. J. Mol. Sci.* **2023**, *24*, 2878. [CrossRef] [PubMed]

10. Sprynskyy, M.; Szczyglewska, P.; Wojtczak, I.; Nowak, I.; Witkowski, A.; Buszewski, B.; Feliczak-Guzik, A. Diatom biosilica doped with palladium(II) chloride nanoparticles as new efficient photocatalysts for methyl orange degradation. *Int. J. Mol. Sci.* **2021**, *22*, 6734. [CrossRef]

11. Royer, S.; Duprez, D.; Can, F.; Courtois, X.; Batiot-Dupeyrat, C.; Laassiri, S.; Alamdari, H. Perovskites as substitutes of noble metals for heterogeneous catalysis: Dream or reality. *Chem. Rev.* **2014**, *114*, 10292–10368. [CrossRef] [PubMed]

12. Royer, S.; Bérubé, F.; Kaliaguine, S. Effect of the synthesis conditions on the redox and catalytic properties in oxidation reactions of LaCo1−xFexO3. *Appl. Catal. A* **2005**, *282*, 273–284. [CrossRef]

13. Kakihana, M.; Yashima, M.; Yoshimura, M.; Ikeda, N.; Sugitani, Y. Synthesis of high surface area LaMnO^{3+}d by a polymerizable complex method. *J. Alloys Compd.* **1999**, *283*, 102–105. [CrossRef]

14. Kim, C.H.; Qi, G.; Dahlberg, K.; Li, W. Strontium-doped perovskites rival platinum catalysts for treating NO$_x$ in simulated diesel exhaust. *Science* **2010**, *327*, 1624–1627. [CrossRef] [PubMed]

15. Russo, N.; Fufori, S.; Fino, D.; Saracco, G.; Specchia, V. Lanthanum cobaltite catalysts for diesel soot combustion. *Appl. Catal. B Enivron.* **2008**, *83*, 85–95. [CrossRef]

16. Peňa, M.A.; Fierro, J.L. Chemical structures and performance of perovskite oxides. *Chem. Rev.* **2001**, *101*, 1981–2018. [CrossRef]

17. Szabo, V.; Bassir, M.; Neste, A.V.; Kaliaguine, S. Perovskite-type oxides synthesized by reactive grinding: Part IV. Catalytic properties of LaCo$_{1-}$$_xFe_xO_3$ in methane oxidation. *Appl. Catal. B Enivron.* **2003**, *43*, 81–92. [CrossRef]

18. Royer, S.; Neste, A.V.; Davidson, R.; Mclntyre, S.; Kaliaguine, S. Methane Oxidation over Nanocrystalline LaCo$_{1-x}$Fe$_x$O$_3$: Resistance to SO$_2$ Poisoning. *Ind. Eng. Chem. Res.* **2004**, *43*, 5670–5680. [CrossRef]

19. Meríno, N.A.; Barbero, B.P.; Grange, P.; Cadús, L.E. La$_{1-}$$_xCa_xCoO_3$ perovskite-type oxides: Preparation, characterisation, stability, and catalytic potentiality for the total oxidation of propane. *J. Catal.* **2005**, *231*, 232–244. [CrossRef]

20. Nie, Y.; Zhang, L.; Li, Y.; Hu, C. Enhanced Fenton-like degradation of refractory organic compounds by surface complex formation of LaFeO$_3$ and H$_2$O$_2$. *J. Hazard. Mater.* **2015**, *294*, 195–200. [CrossRef] [PubMed]

21. Li, S.; Jing, L.; Fu, W.; Yang, L.; Xin, B.; Fu, H. Photoinduced charge property of nanosized perovskite-type LaFeO$_3$ and its relationships with photocatalytic activity under visible irradiation. *Mater. Res. Bull.* **2007**, *42*, 203–212. [CrossRef]

22. Parida, K.M.; Reddy, K.H.; Martha, S.; Das, D.P.; Biswal, N. Fabrication of nanocrystalline LaFeO$_3$: An efficient sol–gel auto-combustion assisted visible light responsive photocatalyst for water decomposition. *Int. J. Hydro. Energy* **2010**, *35*, 12161–12168. [CrossRef]

23. Tang, P.; Tong, Y.; Chen, H.; Cao, F.; Pan, G. Microwave-assisted synthesis of nanoparticulate perovskite LaFeO$_3$ as a high active visible-light photocatalyst. *Curr. Appl. Phys.* **2013**, *13*, 340–343. [CrossRef]

24. Su, H.; Jing, L.; Shi, K.; Yao, C.; Fu, H. Synthesis of large surface area LaFeO$_3$ nanoparticles by SBA-16 template method as high active visible photocatalysts. *J. Nanoparticle. Res.* **2010**, *12*, 967–974. [CrossRef]

25. Tijare, S.N.; Joshi, M.V.; Padole, P.S.; Mangrulkar, P.A.; Rayalu, S.S.; Labhsetwar, N.K. Photocatalytic hydrogen generation through water splitting on nano-crystalline LaFeO$_3$ perovskite. *Inter. J. Hydrogen Engery* **2012**, *37*, 10451–10456. [CrossRef]

26. Libby, W.F. Promising catalyst for auto exhaust. *Science* **1971**, *171*, 499–500. [CrossRef]

27. Safizade, B.; Masoudpanah, S.M.; Hasheminiasari, M.; Ghasemi, A. Photocatalytic activity of BiFeO$_3$/ZnFe$_2$O$_4$ nanocomposites under visible light irradiation. *RSC Adv.* **2018**, *8*, 6988–6995. [CrossRef]

28. Shi, J.; Guo, L. ABO$_3$-based photocatalysts for water splitting. *Prog. Nat. Sci. Mat. Int.* **2012**, *22*, 592–615. [CrossRef]

29. Xu, K.; Feng, J. Superior photocatalytic performance of LaFeO$_3$/gC$_3$N$_4$ heterojunction nanocomposites under visible light irradiation. *RSC Adv.* **2017**, *7*, 45369–45376. [CrossRef]

30. Lu, S.; Wang, G.L.; Chen, S.; Yu, H.T.; Quan, X. Heterogeneous activation of peroxymonosulfate by LaCo$_{1-x}$Cu$_x$O$_3$ perovskites for degradation of organic pollutants. *J. Hazard. Mater.* **2018**, *353*, 401–409. [CrossRef] [PubMed]

31. Gao, P.P.; Tian, X.K.; Nie, Y.L.; Yang, C.; Zhou, Z.X.; Wang, Y.X. Promoted peroxymonosulfate activation into singlet oxygen over perovskite for ofloxacin degradation by controlling the oxygen defect concentration. *Chem. Eng. J.* **2019**, *359*, 828–839. [CrossRef]

32. Rao, Y.F.; Zhang, Y.Y.; Fan, J.H.; Wei, G.L.; Wang, D.; Han, F.M.; Huang, Y.; Croue, J.P. Enhanced peroxymonosulfate activation by Cu-doped LaFeO$_3$ with rich oxygen vacancies: Compound-specific mechanisms. *Chem. Eng. J.* **2022**, *435*, 134882. [CrossRef]

33. Zhu, Y.F.; Liu, Y.F.; Miller, K.A.; Zhu, H.Y.; Egap, E. Lead halide perovskite nanocrystals as photocatalysts for PET-RAFT polymerization under visible and near-infrared irradiation. *ACS Macro. Lett.* **2020**, *9*, 725–730. [CrossRef] [PubMed]

34. Jin, X.Y.; Ma, K.L.; Gao, H.F. Tunable luminescence and enhanced polar solvent resistance of perovskite nanocrystals achieved by surface-initiated photopolymerization. *J. Am. Chem. Soc.* **2022**, *144*, 20411–20420. [CrossRef]

35. Zhu, Y.F.; Liu, Y.F.; Ai, Q.; Gao, G.H.; Yuan, L.; Fang, Q.Y.; Tian, X.Y.; Zhang, X.; Egap, E.; Ajayan, P.M.; et al. In situ synthesis of lead-free halide perovskite–COF nanocomposites as photocatalysts for photoinduced polymerization in both organic and aqueous phases. *ACS Materials Lett.* **2022**, *4*, 464–471. [CrossRef]

36. Koo, P.L.; Jaafar, N.F.; Yap, P.S.; Oh, W.D. A review on the application of perovskite as peroxymonosulfate activator for organic pollutants removal. *J. Environ. Chem. Eng.* **2022**, *10*, 107093. [CrossRef]

37. Courty, P.; Ajot, H.; Marcilly, C.; Delmon, B. Oxydes mixtes ou en solution solide sous forme très divisée obtenus par décomposition thermique de précurseurs amorphes. *Powder Technol.* **1973**, *7*, 21–38. [CrossRef]

38. Baythoun, M.S.G.; Sale, F.R. Production of strontium-substituted lanthanum manganite perovskite powder by the amorphous citrate process. *J. Mater. Sci.* **1982**, *17*, 2757–2769. [CrossRef]

39. Dacquin, J.P.; Dujardin, C.; Granger, P. Surface reconstruction of supported Pd on LaCoO$_3$: Consequences on the catalytic properties in the decomposition of N$_2$O. *J. Catal.* **2008**, *253*, 37–49. [CrossRef]

40. Lisi, L.; Bagnasco, G.; Ciambelli, P.; Rossi, S.D.; Porta, P.; Russo, G.; Turco, M. Perovskite-type oxides: II. Redox properties of LaMn1− xCuxO3 and LaCo$_{1-x}$Cu$_x$O$_3$ and methane catalytic combustion. *J. Solid State Chem.* **1999**, *146*, 176–183. [CrossRef]

41. Zhang, R.; Villanueva, A.; Alamdari, H.; Kaliaguine, S. SCR of NO by propene over nanoscale LaMn$_{1-x}$Cu$_x$O$_3$ perovskites. *Appl. Catal. A* **2006**, *307*, 85–97. [CrossRef]

42. Kaliaguine, S.; Neste, A.V.; Szabo, V.; Gallot, J.E.; Bassir, M.; Muzychuk, R. Perovskite-type oxides synthesized by reactive grinding: Part I. Preparation and characterization. *Appl. Catal. A* **2001**, *209*, 345–358. [CrossRef]

43. Levasseur, B.; Kaliaguine, S. Methanol oxidation on LaBO$_3$ (B = Co, Mn, Fe) perovskite-type catalysts prepared by reactive grinding. *Appl. Catal. A* **2008**, *343*, 29–38. [CrossRef]

44. Alamdari, H.; Royer, S. *Handbook of Perovskites and Related Mixed Oxides, Chapter 2: Mechanochemistry*; Wiley-VCH Verlag GmbH & Co.: Weinheim, Germany, 2016; pp. 25–46.

45. *Properties and Applications of Perovskite-Type Oxides*; Tejuca, L.G.; Fierro, J.L.G. (Eds.) Marcel Dekker: New York, NY, USA, 1992; p. 271.

46. Campagnoli, E.; Tavares, A.; Fabbrini, L.; Rossetti, I.; Dubitsky, Y.A.; Zaopo, A.L. Forni, Effect of preparation method on activity and stability of LaMnO$_3$ and LaCoO$_3$ catalysts for the flameless combustion of methane. *Appl. Catal. B Enivron.* **2005**, *55*, 133–139. [CrossRef]

47. Yang, W.; Zhang, R.; Chen, B.; Bion, N.; Duprez, D.; Hou, L.; Zhang, H.; Royer, S. Design of nanocrystalline mixed oxides with improved oxygen mobility: A simple non-aqueous route to nano-LaFeO$_3$ and the consequences on the catalytic oxidation performances. *Chem. Comm.* **2013**, *49*, 4923–4925. [CrossRef] [PubMed]

48. Chiarello, G.L.; Rossetti, I.; Forni, L. Flame-spray pyrolysis preparation of perovskites for methane catalytic combustion. *J. Catal.* **2005**, *236*, 251–261. [CrossRef]

49. Kleitz, F.; Choi, S.H.; Ryoo, R. Cubic Ia 3 d large mesoporous silica: Synthesis and replication to platinum nanowires, carbon nanorods and carbon nanotubes. *Chem. Comm.* **2003**, *17*, 2136–2137. [CrossRef] [PubMed]

50. Xu, J.; Li, J.; Wu, F.; Zhang, Y. Rapid photooxidation of As(III) through surface complexation with nascent colloidal ferric hydroxide. *Environ. Sci. Technol.* **2014**, *48*, 272–278. [CrossRef]

51. Zhou, D.; Chen, L.; Zhang, C.; Yu, Y.; Zhang, L.; Wu, F. A novel photochemical system of ferrous sulfite complex: Kinetics and mechanisms of rapid decolorization of Acid Orange 7 in aqueous solutions. *Water Res.* **2014**, *57*, 87–95. [CrossRef]

52. Gao, P.; Tian, X.K.; Fu, W.; Wang, Y.X.; Nie, Y.L.; Yang, C.; Deng, Y. Copper in LaMnO$_3$ to promote peroxymonosulfate activation by regulating the reactive oxygen species in sulfamethoxazole degradation. *J. Hazard. Mater.* **2021**, *411*, 125163. [CrossRef]

53. Liu, D.D.; Tang, Y.B.; Hao, Z.K.; Chen, D.Q.; Li, T.Q.; Jiang, L.P.; Tian, B.; Yan, C.P.; Luo, Y.; Jia, B.Y. Comparative study of H$_2$O$_2$/PDS-based advanced oxidation process using nanopaticles for Rhodamine B degradation: Mechanism, stability and applicability. *J. Water. Pro. Eng.* **2022**, *47*, 102757. [CrossRef]